

CNT/PDMS conductive foam-based piezoresistive sensors with low detection limits, excellent durability, and multifunctional sensing capability



Yuxin He^{a,b,c,*}, Xushen Lu^a, Dongyang Wu^a, Mengyang Zhou^a, Guanyu He^a, Jiajia Zhang^a, Li Zhang^d, Hu Liu^{b,c,**}, Chuntai Liu^{b,c}

^a College of Materials Science and Engineering, College of Chemical Engineering and Pharmaceutics, Henan University of Science and Technology, Luoyang, Henan 471023, PR China

^b National Engineering Research Center for Advanced Polymer Processing Technology, Zhengzhou University, Zhengzhou, Henan 450002, PR China

^c Key Laboratory of Materials Processing and Mold (Zhengzhou University), Ministry of Education, Zhengzhou University, Zhengzhou, Henan 450002, PR China

^d College of Chemistry and Chemical Engineering, Luoyang Normal University, Luoyang, Henan 471934, PR China

ARTICLE INFO

Keywords:

CNT
PDMS
Piezoresistive performance
Human health monitoring
E-skin

ABSTRACT

In this paper, a carbon nanotube (CNT)/polydimethylsiloxane (PDMS) conductive composite foam (CCF) was fabricated via a dual-solvent ice template (DSIT) process, whose structure features the conductive filler CNT "embedded" in the cell wall surface, and this CCF was applied to the field of flexible piezoresistive sensing. Benefiting from the sensitive conductive network constructed by the DSIT process, the CNT/PDMS CCF-based piezoresistive sensor can effectively detect compression strains down to 0.1% and exhibits excellent and stable response at compression strains up to 90%. In addition, the CCF shows fast response and recovery times (54 ms and 65 ms), as well as excellent durability and stability (2000 cycles). An electronic skin assembled from the CCF into 5 × 5 pixels was applied to detect the magnitude and spatial distribution of forces and strains. The CCF was also applied for roughness recognition, optical and thermal sensing responses, which shows its potential applications in personalized medical monitoring, electronic smart skin fabrication, external environment monitoring and other fields.

1. Introduction

In recent years, flexible strain sensors have shown promising applications in many fields, such as human movement monitoring [1,2], disease prevention [3,4], electronic smart skin [5–7] and soft robots [8–10]. Conductive polymer composites (CPCs) are widely used to prepare flexible strain sensors due to their excellent flexibility and deformability [11–13]. As an essential flexible strain sensor, flexible piezoresistive sensors can convert the pressure signal into the corresponding resistance signal [14–16], and have been widely studied for their advantages of easy signal acquisition, simple application process, low cost, and excellent sensing performance [15,16]. In order to meet the requirements of full-scale human motion detection from minor

strains (e.g., pulse and swallowing) to large strains (e.g., arm bending and joint movements), there is still an urgent need for flexible piezoresistive sensors with high sensitivity, wide operating sensing range, and fast response time.

In general, one of the effective ways to improve the sensitivity of the piezoresistive sensor is to construct a typical microstructure [17,18]. Flexible porous materials have been widely studied in piezoresistive strain sensors because of their unique porous structure, low relative density, high specific strength, and high specific surface area [19–21]. Many methods have been reported for the controlled induction of porous structures in flexible polymer matrices, such as solution-evaporation process [22], salt template process [23], sugar template process [24], sandpaper template process [25], and ice template process [26], etc. The

* Corresponding author at: College of Materials Science and Engineering, College of Chemical Engineering and Pharmaceutics, Henan University of Science and Technology, Luoyang, Henan 471023, PR China.

** Corresponding author at: National Engineering Research Center for Advanced Polymer Processing Technology, Zhengzhou University, Zhengzhou, Henan 450002, PR China.

E-mail addresses: heyx@haust.edu.cn (Y. He), liuhu@zzu.edu.cn (H. Liu).

ice template process is a method for preparing porous materials, which can effectively control the formation of three-dimensional porous structure in one direction of the porous material. Zhai et al. [27] applied an ice-template process to prepare carbon black (CB) modified thermoplastic polyurethane (TPU) foam, which shows a pinnate-vein-arranged porous structure and excellent flexibility. The SEM results showed that the conductive CB particles were distributed in porous skeleton of the foam with a gauge factor (*GF*) of 1.55. The response/relaxation time of the prepared foam was 150/150 ms. Ma et al. [28] applied ice-template process to prepare graphene modified porous TPU foam with low density and high electrical conductivity. Benefit from the excellent elasticity and high porosity of the composite, it exhibited a stable piezoresistive sensing signals and good compressibility under 90% compression strain.

These results indicate that the ice-template process can build three-dimensional microstructures in flexible CPCs substrates and endow it

with good sensing stability [29,30], high flexibility, and wide sensing range [31,32], but its poor ability to detect slight strains hinders its wide application. Therefore, it remains a challenge to improve the sensitivity of flexible piezoresistive sensors, especially the response under slight strains. If the conductive filler is dispersed in the interfacial phase of the oil-in-water emulsion, flexible CPCs with conductive filler "embedded" in the cell wall surface can be prepared by the ice template process. When the cell wall is slightly deformed, its resistance changes significantly, which is expected to improve the sensitivity of piezoresistive sensors.

Herein, carbon nanotube (CNT)/polydimethylsiloxane (PDMS) conductive composite foam (CCF) was successfully prepared in this study using a dual-solvent ice template (DSIT) process. By adjusting the distribution of the conductive filler CNT in the interfacial phase of the oil-in-water emulsion, a unidirectional lyophilization process was used to achieve the "embedding" of CNT on the surface of the cell wall, and a

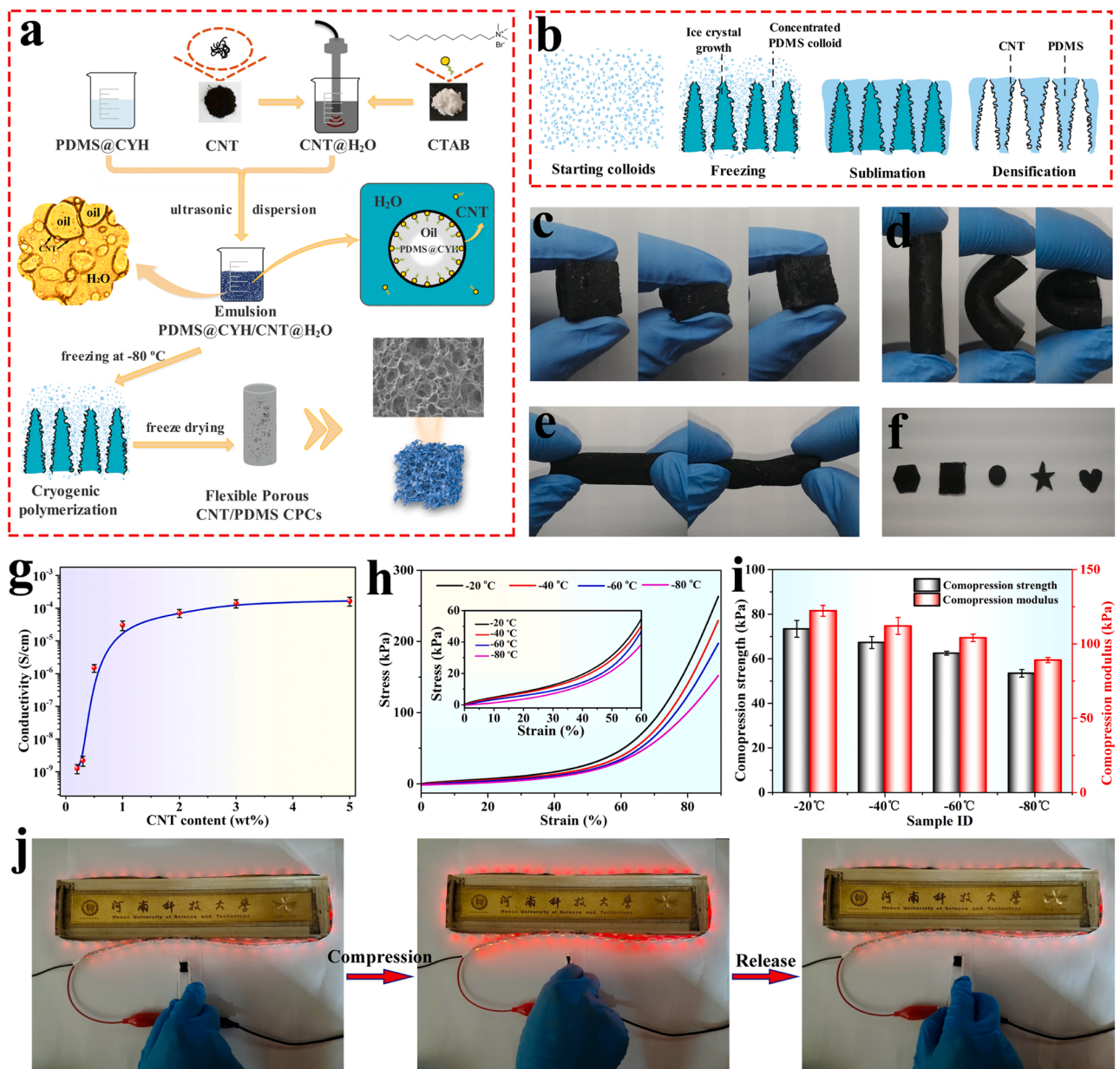


Fig. 1. (a) Schematic diagram of the preparation CNT/PDMS CCF. (b) Schematic diagram of DSIT process. Digital images showing the flexible porous CNT/PDMS CCF can withstand (c) high level of compression, (d) bending, (e) twisting and (f) tailor. (g) Conductivity of CNT/PDMS CCF with 1.0 wt% CNT loadings. (h) Stress vs. strain curves, (i) compression strength and modulus of CNT/PDMS CCF with 1.0 wt% CNT under different forming temperature at a compression rate of 5 mm/min. (j) The light intensity variation of LED connected with the CNT/PDMS CCF.

sensitive conductive network was constructed on the surface of the PDMS skeleton. The sensing range, sensitivity and cyclic compression sensing performance of the prepared CNT/PDMS CCF were systematically investigated. Then, the CCF-based piezoresistive sensor was used to monitor the full range of human motion and weak physiological signals, and its applicability was evaluated. Finally, the CCF-based piezoresistive sensors are demonstrated for applications in electronic skin (e-skin), recognition of texture features on object surfaces, and optical and thermal sensing.

2. Experimental

2.1. Materials

PDMS (601-A, 98.0 wt%, CP) and the curing agent (601-B, 98.0 wt%, CP) were purchased from Beijing Hibest Technology Limited Company, China. Cyclohexane (CYH, 99.5 wt%, CP) and cetyltrimethylammonium bromide (CTAB, 99.5 wt%, CP) were obtained from Tianjin Chemical Reagent Limited Company, China. Multi-walled carbon nanotube (CNT, TNM0, 98.0 wt%) was purchased from Shandong Zhanda Reagent Limited Company, China. Conductive copper paste (NX-515, Tech) was purchased from Shenzhen Guangpiao Electronic Material Limited Company, China. All materials were used as received without any further purification.

2.2. Preparation of CNT/PDMS CCF

The CNT/PDMS CCF was prepared via a dual-solvent ice-template (DSIT) process. Fig. 1a shows a schematic diagram of the DSIT process. Firstly, 0.027 g CNT was ultrasonically dispersed in 12.0 g deionized water containing 0.04 g emulsifier CTAB to obtain a black dispersion (CNT@H₂O). Secondly, 2.0 g PDMS was completely dissolved in 6.0 g CYH to get a milky solution (PDMS@CYH). Thirdly, the uniformly dispersed oil-in-water emulsion was obtained by adding PDMS@CYH solution to CNT@H₂O black dispersion and ultrasonic dispersion at 40 °C for 30 min (Fig. S1). Fourthly, 0.7 g curing agent was added into the emulsion and shaken well. Fifthly, the emulsion was transferred to a refrigerator at -80 °C for 72 h to allow complete freezing and crystallization. Finally, the CNT/PDMS CCF was prepared after vacuum drying at -70 °C for 72 h.

2.3. Characterization

The morphology of PDMS/CYH@CNT/H₂O emulsion was performed with an optical microscope (Olympus BX53). Carl Zeiss Sigma 500 field emission scanning electron microscopy was adopted to characterize the micromorphology of pure PDMS and CNT/PDMS CCF. X-ray diffraction (XRD) patterns in the 2θ range of 10°~50° were recorded by a D8 ADVANCE diffractometer (Bruker Instruments Co., Germany). Fourier transform infrared (FTIR) spectroscopy (Nicolet Nexus 870, Thermo Fisher Scientific, USA) was conducted in the range of 500–4000 cm⁻¹. Thermogravimetric analysis (TGA) was performed on a TGA 2 (Mettler Toledo Instruments Co., Switzerland) system from room temperature to 700 °C with heating rate of 10 °C/min under nitrogen atmosphere. Differential scanning calorimetry (DSC 200F3, Netzsch Instruments Co., Germany) was applied to characterize the glass transition temperature (T_g) and melting point (T_m) of CCF. The conductivity of CCF was measured via a digital multimeter (DMM4040, Tektronix Technology Co., Ltd., China). The mechanical performance of CCF was assessed by a single-column micro-control electronic universal testing machine (WWD-1D, Jilin Guangtian Technology Co., Ltd., China) [33]. The piezoresistive sensing performance of CCF was evaluated by self-built equipment in the laboratory, as shown in Fig. S2. I-V curves of CCF under different strain/pressure were tested by a Princeton ParStat4000 + electrochemical workstation (AMETEK shanghai trading Co., Ltd., China). Pressure sensitivity S ($S = -(\Delta R/R_0)/P$, where P

represents the applied pressure [34,35]) was adopted to evaluate the pressure response of CCF.

3. Results and discussion

3.1. Conductivity, mechanical properties and structure of the CCF

Fig. 1b shows the schematic diagram of the mechanism for preparing CNT/PDMS CCF by DSIT process. The mixture of CNT@H₂O and PDMS@CYH is converted into a uniformly dispersed oil-in-water emulsion due to the strong ultrasonic dispersion effect of the ultrasonic cell crusher. During the cooling process, PDMS is ejected from the cyclohexane crystals and CNT is also ejected from the aqueous phase crystals [36,37]. PDMS and CNT are enriched, fused and solidified at the interface of the dual-solvent phase. The crystals formed by solvent molecules at low temperature are sublimated in the freeze dryer and extracted directly from the composite framework, where the space previously occupied by the crystals becomes pore space instead. Finally, a porous structure with CNT embedded on the cell wall surface is achieved. Clearly, the prepared CNT/PDMS CCF by DSIT process exhibits excellent compressibility (Fig. 1c), bendability (Fig. 1d), twistability (Fig. 1e), and tailorability (Fig. 1 f). All of these properties give CCF the excellent performance required as a piezoresistive sensor.

Excellent conductivity and mechanical properties are essential prerequisites for flexible porous CNT/PDMS CCF as a piezoresistive sensor. Fig. 1g shows the effect of CNT loadings on the conductivity of CCF. The conductivity of CCF increases significantly from 1.26×10^{-9} S/cm to 3.06×10^{-4} S/cm when the CNT loading is increased from 0.2 wt% to 1.0 wt%, and then stabilizes with further increase of CNT loading, indicating that a stable and sensitive conductive network has been formed inside the CCF with 1.0 wt% CNT loading. As depicted in Fig. S3, the conductivity of CCF stabilizes with time at 43% relative humidity; the conductivity of CCF shows an increasing trend with increasing ambient relative humidity, which can be attributed to the growing concentration of adsorbed water molecules on the surface of CCF. Fig. 1h and 1i show the compression performance of CCF prepared by the DSIT process at different freeze-forming temperatures with 1.0 wt% CNT loading. Obviously, the stress of CCF increases slowly with increasing compression strain and always remains at a low value when the compression strain is less than 60%; it increases sharply after an inflection point in the strain range of 60–75%, which is mainly caused by the change of three-dimensional structure of CCF during compression. Besides, the stress of CCF decreases with decreasing freeze-forming temperature, which is related to the domain size of ice crystal phase formed by the dual-solvent system at different temperatures. As decreasing freeze-forming temperature, the domain size of ice crystal formed by the crystallization of the dual-solvent phase gradually decreases, resulting in an increase of the porosity (Table S1) and a decrease of strength for CCF. As shown in Fig. 1i, the strength and modulus of CCF are very low in the compression strain range of 0–60%. Notably, the compression strength and modulus of CCF prepared at -80 °C were only 38.3 kPa and 51.4 kPa, respectively. Such a forming temperature-dependent mechanical performance can be explained based on the SEM images shown in Fig. S4, where the prepared CCF all have honeycomb-shaped cells. As decreasing the freeze-forming temperature, the porosity of CCF increases, the cell walls are thinner, and the distance between cells becomes smaller. As depicted in Fig. S5 and Table S2, it can be seen that the CCF has a small hysteresis at 20% strain (1.23%), which indicates that the CCF is able to spring back quickly after receiving a stimulus. The hysteresis of the CCF at 80% strain is only 11.9%, which is lower than most reported strain sensors [38]. This is due to the good elasticity of the PDMS matrix itself, and the unique structure of CNT "embedded" in the cell walls of the CCF, which avoids the mismatch between the filler and the polymer due to the difference in modulus, thus demonstrating the low hysteresis of the CCF.

Furthermore, the effect of CNT loading on the mechanical

performances of flexible porous CNT/PDMS CCF prepared by the DSIT process at -80°C is discussed. As depicted in Fig. S6, the maximum compression strength and modulus of CCF increase significantly with increasing CNT loading. On the one hand, CNT has high strength and modulus; on the other hand, CNT is uniformly dispersed in the PDMS matrix. The good interfacial adhesion between CNT and PDMS matrix facilitates stress transfer between PDMS and CNT during compression [39,40]. Considering the stable conductivity and mechanical properties, the CCF prepared at -80°C with 1.0 wt% CNT loading was applied for the subsequent study. Finally, the prepared CCF was connected to the circuit of red light-emitting diodes (LEDs) to demonstrate its piezoresistive sensing effect (Fig. 1j). Clearly, the illumination of LEDs increases when external pressure is applied to CCF, and becomes normal after the pressure is removed. All these indicate the great potential of our prepared CNT/PDMS CCF as a piezoresistive sensor.

Then, the microstructures of pure PDMS and CNT/PDMS CCF prepared by the DSIT process were systematically investigated. Figures 2a-

a₂ show the SEM images of pure PDMS foams. It can be observed that the cell diameter of pure PDMS foam is about 60 μm and there are many incomplete micropores in the cell wall, which reduces the strength and stability of the foam [41,42]. For CNT/PDMS CCF, as shown in Figures 2b-b₂, the cell diameter is similar to that of pure PDMA foam, indicating that the addition of CNT does not affect its cell size. It is worth mentioning that there are no micropores in the cell walls of CCF with CNT adding, indicating that the introduction of CNT helps to improve the integrity of its porous structure [36]. This is mainly attributed to the steric hindrance effect of CNT and the interaction between CNT and PDMS effectively preventing the contraction of PDMS molecular chains due to the sublimation of solvent ice crystals [37]. In addition, CNT was uniformly dispersed on the cytoskeleton surface without agglomeration (Figures 2b₃-b₅), constructing an effective and sensitive conductive network in CCF. Uniformly dispersed CNT and an intact porous structure in the matrix are necessary conditions for CCF to obtain a stable electrical response signal.

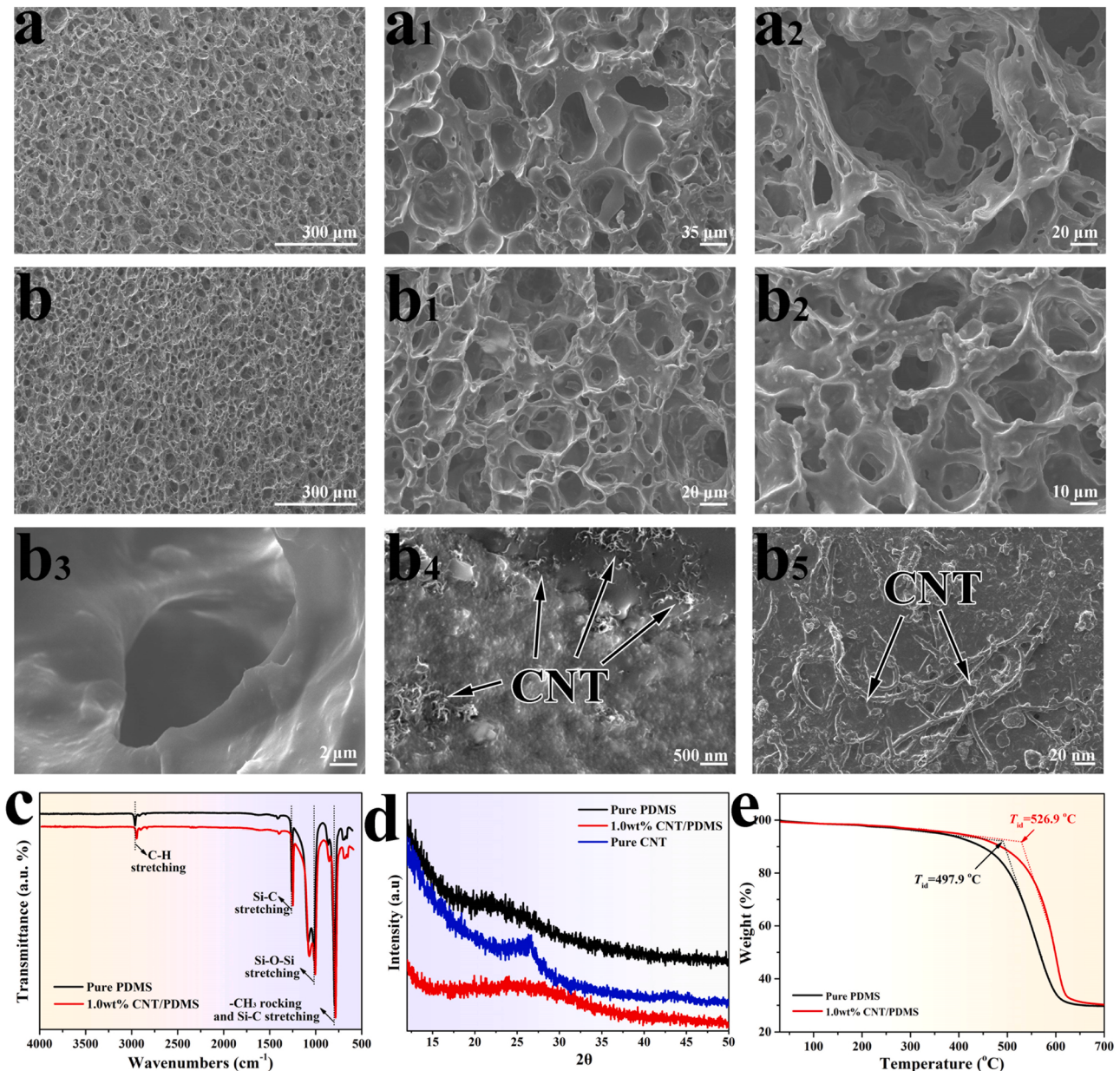


Fig. 2. SEM images of (a~a₂) pure PDMS foam and (b~b₅) CNT/PDMS CCF at different magnifications. (c) FTIR spectra, (d) XRD patterns, and (e) TG curves of pure PDMS foam and CNT/PDMS CCF.

The interactions between CNT and PDMS were further characterized by FT-IR and XRD. For the FTIR spectrum of pure PDMS shown in Fig. 2c, the band near 794 cm^{-1} is assigned to Si-C stretching and -CH₃ shaking in the Si-CH₃ group. The band near 1016 cm^{-1} is assigned to Si-O-Si stretching. In addition, the bands near 1259 cm^{-1} and 2962 cm^{-1} are attributed to Si-C and C-H stretching, which are considered as -CH₃ deformation in Si-CH₃ and -CH₃ asymmetric stretching in Si-CH₃, respectively [43]. Comparing with pure PDMS, the bands of CNT/PDMS CCF generally shift to low wavenumbers, that is, the blue-shift occurs, indicating a strong interaction between CNT and PDMS [44]. The XRD patterns of CNT, pure PDMS and CNT/PDMS CCF are shown in Fig. 2d. Obviously, pure PDMS shows no characteristic diffraction peak in the range of $15^\circ\sim50^\circ$, which is due to the fact that PDMS is in the amorphous phase region within the diffraction range [45]. Moreover, the CNT/PDMS CCF shows a weak and wide diffraction peak at 22.5° , and the (002) diffraction peak is not observed at 26.5° for the hexagonal graphite of CNT, which can be ascribed to the homogeneous dispersion of CNT and the strong interaction between CNT and PDMS matrix [46].

The thermal properties of pure PDMS and CNT/PDMS CCF were characterized. Fig. 2e and S7 show their TGA and DTG curves, and the initial decomposition temperature (T_{id}), maximum decomposition temperature (T_p) and residual carbon content of them are listed in Table S3. Obviously, pure PDMS and CNT/PDMS CCF show similar thermal decomposition properties, and the T_{id} and T_p of them are $497.9\text{ }^\circ\text{C}$ and $526.4\text{ }^\circ\text{C}$, $545.5\text{ }^\circ\text{C}$ and $584.7\text{ }^\circ\text{C}$, respectively, indicating that the introduction of CNT into PDMS matrix can effectively improve the thermostability of CCF. Fig. S8 shows the DSC curves of pure PDMS foam and CNT/PDMS CCF, and the glass transition temperature (T_g) and melting temperature (T_m) of them are shown in Table S4. The T_g and T_m of pure PDMS and CNT/PDMS CCF are $-124.3\text{ }^\circ\text{C}$ and $-41.6\text{ }^\circ\text{C}$, $-121.7\text{ }^\circ\text{C}$ and $-38.8\text{ }^\circ\text{C}$, respectively, indicating that the introduction of CNT to PDMS matrix reduces the flexibility of the CCF molecular chain, which can be attributed to the physical cross-linking effect of CNT in the matrix and limiting the free motion ability of PDMS molecular chains [47,48]. The characterization of the thermal properties of the prepared CCF demonstrates the successful introduction of the

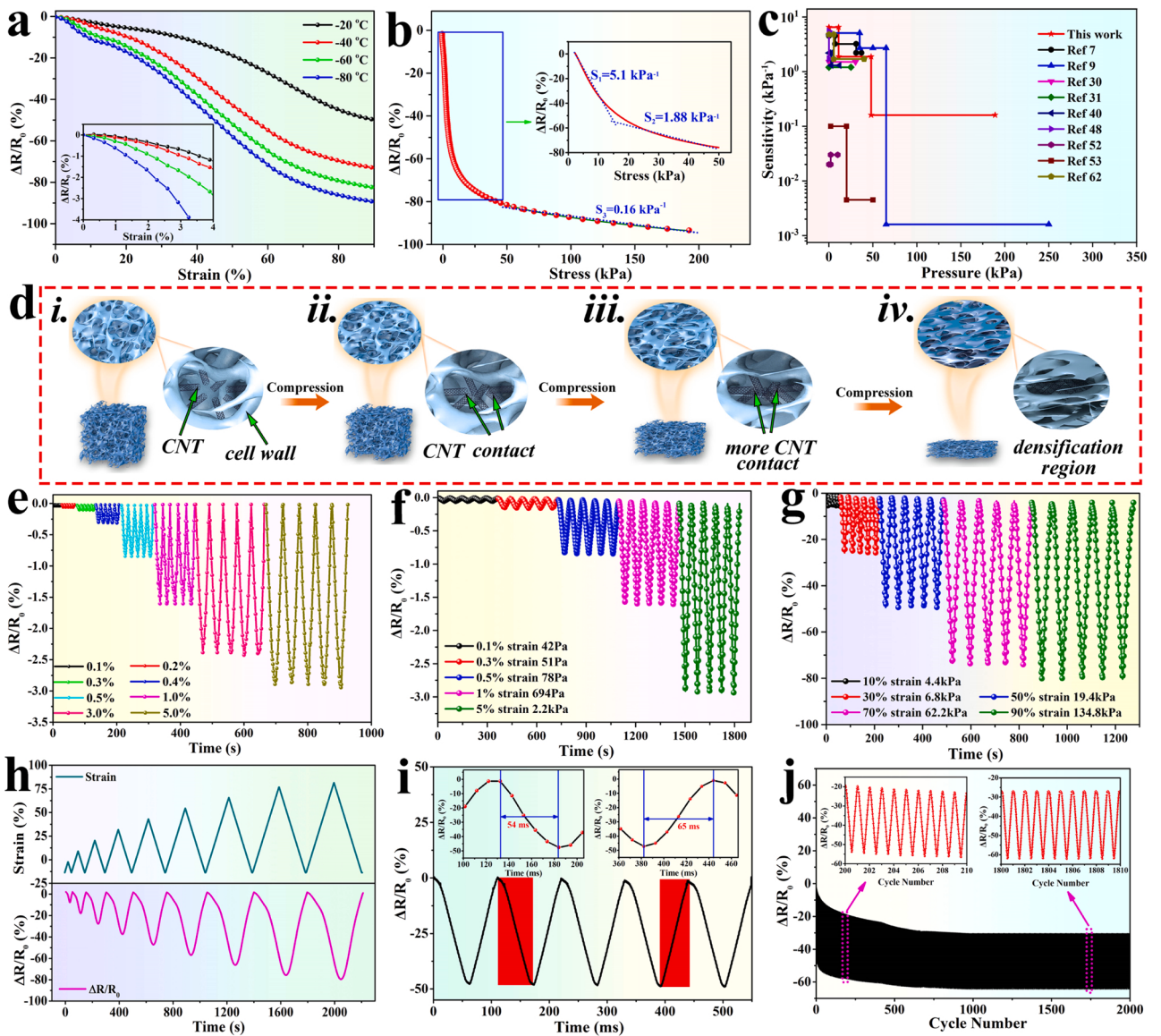


Fig. 3. $\Delta R/R_0$ vs. (a) strain curves of different freeze-forming temperature and (b) pressure curves for CNT/PDMS CCF. (c) Comparison of sensitivity and pressure sensing range of the CCF with other previously reported piezoresistive pressure sensors. (d) Schematic diagram of the piezoresistive sensing mechanism for CNT/PDMS CCF. Cyclic piezoresistive sensing properties of CNT/PDMS CCF (e,f) under different compression strain/pressure levels at a compression rate of 5.0 mm/min and (g) at different compression rates under 50% strain. (h) Stepwise piezoresistive sensing behavior of CNT/PDMS CCF up to 90% strain. (i) The response and recovery time of CNT/PDMS CCF at 50% strain. (j) Cyclic piezoresistive sensing performances of CNT/PDMS CCF at 50% strain over 2000 cycles.

conductive filler CNT into the PDMS matrix, which is also a proof of the successful preparation of the structure for CNT embedded on the PDMS cell wall.

3.2. Piezoresistive sensing performance of the CCF

The excellent electrical conductivity, mechanical performance and microstructure of CNT/PDMS CCF provide a solid foundation for its potential applications as the wearable piezoresistive sensor. Fig. 3a shows the $\Delta R/R_0$ ($\Delta R/R_0 = (R-R_0)/R_0$) vs. compression strain curves of CCF prepared at different freeze-forming temperatures, where R and R_0 represent the instantaneous resistance and initial resistance, respectively [49,50]. Clearly, the $\Delta R/R_0$ values of all CCF show the same trend in the strain range of 0–90%, and the $\Delta R/R_0$ values of CCF prepared at -80°C vary significantly under slight strain, mainly due to the evolution of its microstructure. As decreasing the freeze-forming temperature, the porosity of CCF increases, the cell wall becomes thinner, and the intercellular distance becomes smaller; the cell wall shape of CCF changes under slight pressure, leading to significant changes in the resistance values.

Subsequently, the piezoresistive response behavior of CCF-based pressure sensor prepared at -80°C with 1.0 wt% CNT was systematically studied. Based on the stress vs. strain curves (Fig. 1 h), the $\Delta R/R_0$ vs. pressure curves of CCF were also plotted (Fig. 3b). Clearly, the values of $\Delta R/R_0$ exhibit a sharp decrease and then stabilize over the entire pressure range (49.7–189.2 kPa). Specially, S values of the CCF can be divided into three parts: 5.1 kPa^{-1} , 1.88 kPa^{-1} and 0.16 kPa^{-1} , corresponding to the pressure ranges of 0–9.2 kPa, 9.2–49.7 kPa and 49.7–189.2 kPa, respectively. As shown in Fig. 3c and Table S5, the prepared CCF-based piezoresistive sensor showed superior sensing performance than other reported works [51–54].

The piezoresistive response mechanism of the CCF can be explained by the conclusions shown in Fig. 3d and S9. In generally, the change of the CCF's conductive network under external pressure plays a crucial role in the piezoresistive response behaviors. When no pressure is applied, the resistance of CCF is mainly composed of R_{foam} of the whole foam skeleton (Figures 3d-i and S9a-a₂). When small pressure is applied to the CCF, the deformation of the foam skeleton causes contact between conductive fillers distributed on the cell wall surface, forming a large number of conductive networks (Figures 3d-ii and S9b-b₂). This leads to a sharp decrease of R_{foam} , resulting in higher S values. When CCF is further compressed, the contact area (including the contact of cell wall and the contact of conductive fillers) increases further (Fig. 3d-iii and S9c-c₂), but the conductive network saturates, resulting in a decrease in the growth of R_{foam} . Herein, the value of S decreases. With further increasing the pressure, the CCF enters the dense region (Figure 3d-iv and S9d-d₂), and R_{foam} basically remains unchanged, so the S value stabilizes.

After that, the cyclic piezoresistive performance of CCF-based sensor is also systematically characterized. In Fig. S10, the I-V curves of CCF under different compression strains show the good linear ohmic behavior, indicating its stable electrical properties, which are conducive to stable signal output. As shown in Figs. 3e and 3f, the CCF exhibits outstanding stable and repeatable sensing patterns under different strain/pressure. Notably, a slight pressure change of 42 Pa under 0.1% compression strain is effectively detected, showing ultra-high discernibility. In addition, the CCF still exhibits excellent and stable response behavior at 90% compression strain per 135 kPa, indicating a wide strain detection range. Meanwhile, a stable and repeatable sensing pattern of the sensor was observed at different compression rates (Fig. 3g), indicating a compression rate dependence of its responsiveness. From Fig. 3f and 3g, it can be seen that the response curve of CCF-based strain sensor has a baseline drift phenomenon. The baseline drift of the response curve for the strain sensor is affected by many conditions such as the strength of the response signal and the stretch-relaxation rate [55]. The smaller the strength of the response signal, the more

pronounced the signal drift. The greater the tensile-relaxation rate, the more pronounced the signal drift. The tensile-relaxation rate at large cyclic strains is higher than that at small cyclic strains, resulting in a higher baseline drift of the response signal at 5% cyclic strains than at 0.1% cyclic strains (Fig. 3 f) and at 90% cyclic strains than at 10% cyclic strains (Fig. 3 g). Fig. 3 h shows the stepwise cyclic piezoresistive sensing performance of the sensor in the compression strain range of 10–90%. Clearly, the maximum $\Delta R/R_0$ value of CCF increases with increasing the compression strain and returns to the initial value after the external compression is relieved, indicating that it has a suitable identification and recoverability for various compression strain levels. As depicted in Fig. 3i, the response time and the recovery time of the CCF are 54 ms and 65 ms, respectively, indicating that the CCF has rapid response characteristics. The rapid response characteristics of CCF can be attributed to unique conductive network of CNT "embedded" on the surface of the cell wall inside CCF. When the sensor is compressed by the outside world, the resistance of the system will change significantly even if the cell wall is slightly deformed. During the rebound of the sensor, the new conductive network formed by the compressed contact of the pore wall is destroyed and returns to its original state. During the rebound of the sensor, the new conductive network formed by the compression of the cell wall contact will be destroyed and return to its original state. CCF has a low hysteresis, as depicted in Table S2. Therefore, CCF has rapid response characteristics. Finally, the CCF also shows good stability and recoverability after 2000 compression cycles (Fig. 3j), which is supported by its excellent compression mechanical properties shown in Fig. S11.

3.3. Applications

3.3.1. Human movement and health monitoring

Based on the wide piezoresistive response range and high response sensitivity of the prepared CNT/PDMS CCF, it is expected to be a candidate sensor for real-time detection of the full range of human movement. To demonstrate the promising application of the CCF, it was attached to a volunteer's knee (Fig. 4a), elbow (Fig. 4b), wrist (Fig. 4c) and finger (Fig. 4d) by medical tape to detect joint movements. Obviously, the CCF can output stable cyclic sensing signal under a fixed bending angle, and the responsiveness increases with increasing the bending angle, indicating its ability to detect different bending motions. As shown in Fig. 4e, the CCF has excellent signal responsiveness and stability when it is pressed rapidly at specific time intervals, providing technical support for detecting rapid human motion and predicting early Parkinson's disease [56,57].

In addition, the CCF has been applied to test the tiny deformation of the human body. As shown in Fig. 4f, when the CCF was attached to the bicipital muscle of arm, its response signals increased with muscle contraction and recovered to the initial value after relaxing the muscle, demonstrating its potential application in guiding human training and injured muscle recovery [58]. As shown in Fig. 4g, when the CCF was fixed on the laryngeal node of a volunteer, it outputted stable and regular sensing signals with the reciprocal movement of the laryngeal node, indicating its excellent development potential in monitoring of the fine activity of organs. Here, as shown in Fig. 4h, the CCF can also be used to monitor the pulse signal of human body and obtain a regular sensing signal. In detail, the volunteer's pulse is calculated as 72 beats per minute, which is within the range of average human pulse level. In addition, Fig. 4i exhibits a zoomed-in plot of one pulse signal, where three response peaks of the percussion wave (P1), the tidal wave (P2) and the dicrotic wave (P3) were observed [52], indicating the excellent fast response and sensitivity of the CCF. Based on the above discussion, it is proved that the CNT/PDMS CCF-based piezoresistive sensor shows great potential applications in human health and movement monitoring.

3.3.2. The artificial electronic skin (e-skin)

Based on the outstanding resilience and piezoresistive response of

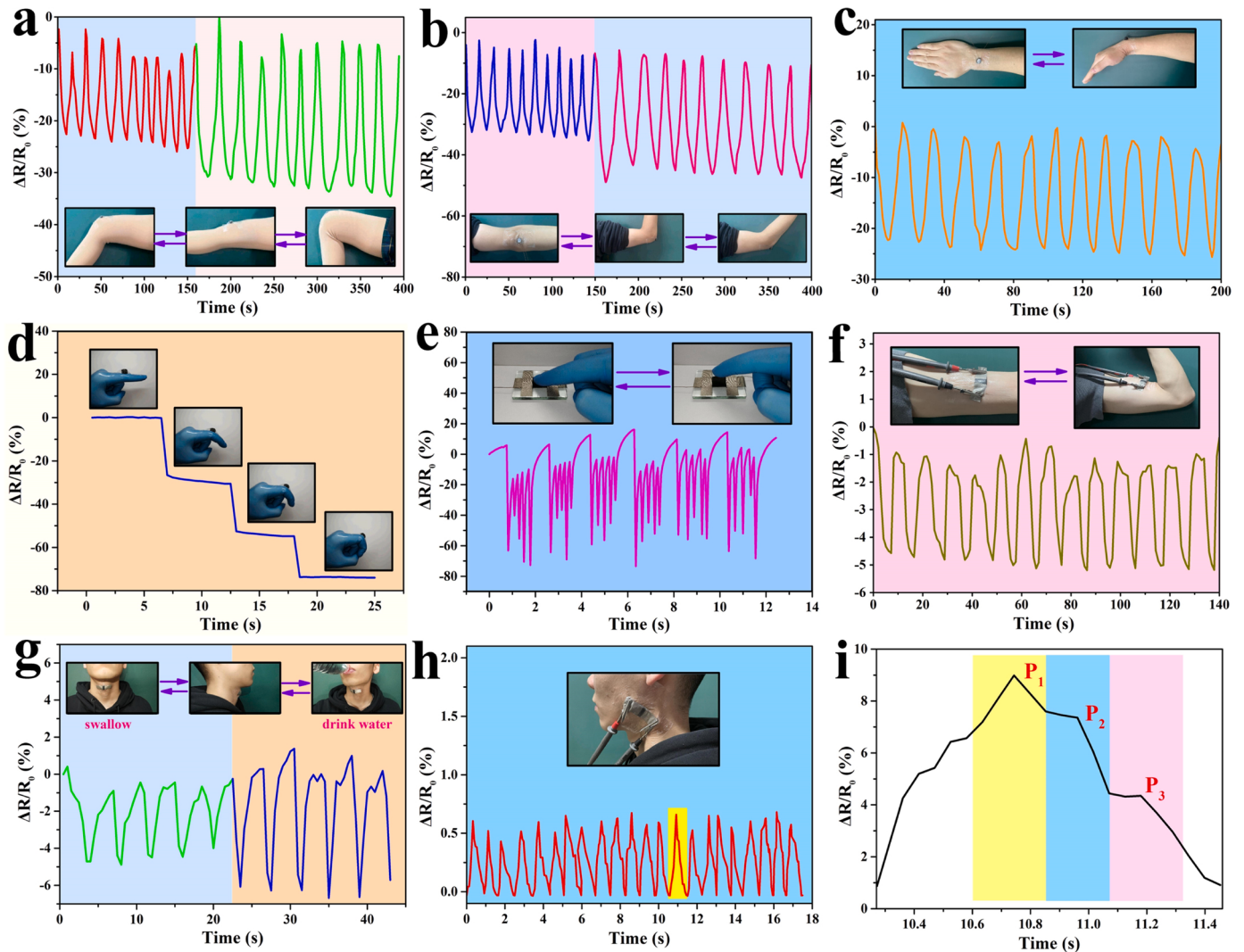


Fig. 4. Sensing performances of the CNT/PDMS CCF served as a strain/pressure sensor for the real-time detection of (a) knee bending, (b) elbow bending, (c) wrist bending and (d) finger bending. (e) Real-time sensing signal of CNT/PDMS CCF for pressing quickly within a certain time interval, (f) brachioradialis of the forearm for tensioning and relaxing, (g) swallowing and drinking, and (h,i) wrist pulse.

prepared CNT/PDMS CCF, it was also integrated into a 5×5 pixels sensory array to study its application in artificial electronic skin (e-skin). The CCF was first cut into a cylinder with 10 mm height and a diameter of 10 mm, and coated with conductive silver paste at both ends to eliminate contact resistance. Then, the cylinder was integrated into 5×5 pixels and finally electrodes were attached at both ends. Fig. 5 shows the sensing performance of the e-skin assembled based on CCF. As expected, when the weight with a certain mass was placed on the e-skin (Fig. 5a), the electrical output of the corresponding sensor could be recorded in real-time, and the pressure distribution was displayed by the 2D mapping (Fig. 5 a₁) and 3D mapping (Fig. 5 a₂), respectively. Similarly, when two glass columns with the same mass were placed on the e-skin in different shapes (Figs. 5b and 5c), the pressure distribution and the position could also be recognized from the sensing response mapping (Fig. 5 b₁~b₂, c₁~c₂), indicating the great potential of CNT/PDMS CCF-based piezoresistive sensor on e-skin.

3.3.3. Other sensing applications

Roughness identification, optical and thermal sensitivity of the prepared CNT/PDMS CCF were further investigated to explore its other potential applications. Figures 6a and S12a-a₂ show the schematic and digital photograph of reciprocating friction test between CCF and sandpaper with different roughness. Adhere sandpaper to the bottom of

the weight, and pull the weight back and forth through the string to make the sandpaper make a reciprocating friction movement on the surface of CCF. Figure 6a₁ shows the $\Delta R/R_0$ vs. time curves of CCF when sandpaper with different meshes (Fig. S13) passes over CCF surface in 30-second intervals. Clearly, the $\Delta R/R_0$ value increases when sandpaper passes over the surface of CCF and decreases when the sandpaper stops sliding. With increasing sandpaper mesh, the $\Delta R_{max}/R_0$ value shows an increasing trend. The larger the meshes of sandpaper, the smaller the gap between sandpaper abrasives. When the sandpaper slides, the greater the occluding degree between the abrasive and the microstructure of the CCF surface, resulting in the stronger response signals.

Fig. 6b and S12b~b₂ show the schematic and digital photos of the method for optical sensing performance of the CNT/PDMS CCF. The height of the xenon lamp was adjusted to simulate different light intensities (14.5 cm, 9.5 cm and 7.2 cm are similar to 1, 3 and 5 light intensities, respectively) [59,60]. Figure 6b₁ shows the $\Delta R/R_0$ vs. time curves of CCF irradiated with different light intensities at 30-second intervals. Clearly, its $\Delta R/R_0$ value tends to decrease when the light source irradiates CCF; the $\Delta R/R_0$ value increases when the light source is turned off; the response of CCF also increases with the increase of light intensity. The response behavior of CCF after being exposed to light can be attributed to the increase of the carrier concentration [61], resulting in a lower resistance.

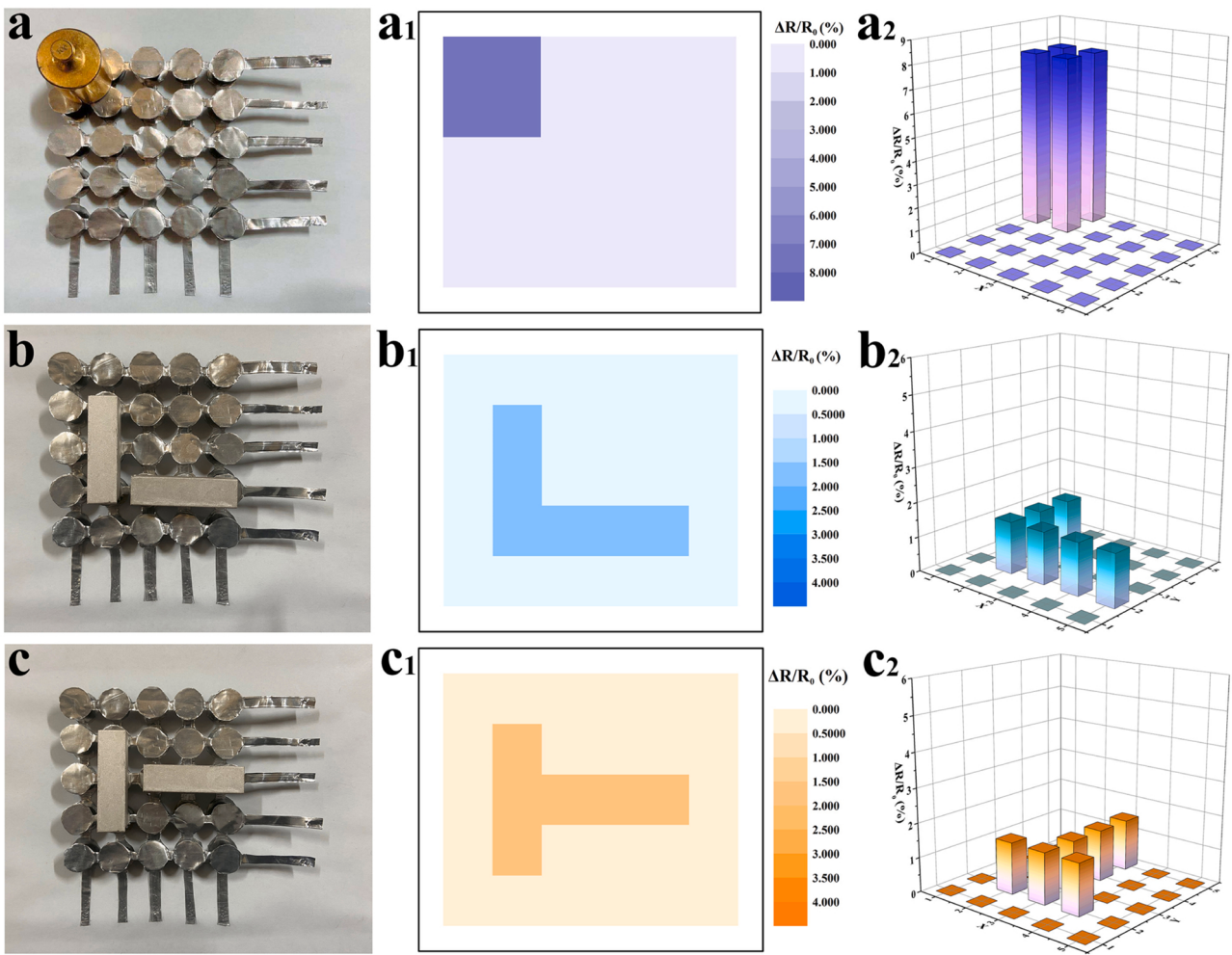


Fig. 5. (a) Photograph of a 100 g weight lying onto the E-skin assembled from the CNT/PDMS CCF-based pressure sensor with 5 × 5 pixels and (a₁, a₂) the corresponding pressure sensing mapping based on the current variation. (b, c) Photograph of two glass columns with the same mass lying onto the E-skin in different shapes and (b₁, b₂, c₁, and c₂) the corresponding pressure sensing mapping based on the current variation.

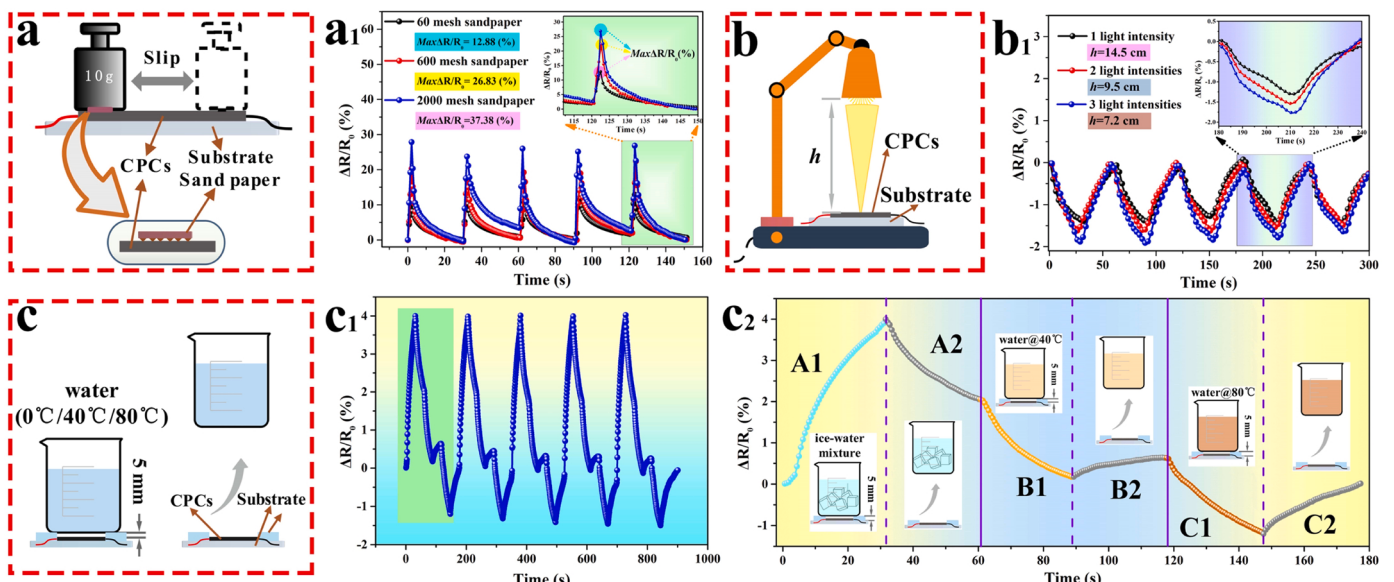


Fig. 6. The applications of prepared CNT/PDMS CCF in (a) frictional sensing, (b) optical sensing and (c) thermal sensing behavior. $\Delta R/R_0$ vs. time curves of CCF (a₁) for reciprocating friction on sandpaper, (b₁) irradiated by different light intensities at 30 s interval, (c₁) irradiated by different thermal intensities at 30 s interval with the non-contact thermal mode and (c₂) one temperature cycle curve.

For the thermal sensing performance of CCF, the non-contact mode was systematically investigated at the room temperature, and the test method is schematically shown in Fig. 6c and S12c~c₂. As shown in Figure 6c₁, the CCF exhibited different response when beakers filled with water at 0 °C, 40 °C and 80 °C were sequentially circulated to 5 mm above it. The response curves of one thermal cycle are shown in Figure 6c₂. It can be observed that the values of $\Delta R/R_0$ for CCF exhibits an increasing trend when the beaker filled with ice-water mixture at 0 °C approaches the CCF (A1). When the beaker is removed, the $\Delta R/R_0$ gradually recovers (A2). However, the $\Delta R/R_0$ exhibits a decreasing trend when the beaker filled with 40 °C water approaches the CCF (B1). The $\Delta R/R_0$ gradually recovers when the beaker is removed (B2). The $\Delta R/R_0$ decreases faster than that of the 40 °C heat source when the beaker filled with 80 °C water approaches the CCF (C1). The $\Delta R/R_0$ gradually recovers when the beaker is removed (C2). The thermal response behavior of the CCF at different temperatures can be attributed to its intrinsic negative temperature coefficient of resistance (TCR) effect, which is consistent with the literature [62]. In summary, the prepared CNT/PDMS CCF has enormous potential applications in advanced flexible smart electronic skins and human-machine interfaces for next-generation wearable electronic devices.

4. Conclusions

In this paper, carbon nanotube (CNT)/polydimethylsiloxane (PDMS) conductive composite foam (CCF) was prepared by a dual-solvent ice template (DSIT) process. During the preparation, CNT was dispersed at the interfacial phase of the oil-in-water emulsion and then embedded in the cell wall surface of PDMS during the curing process, where a sensitive network was constructed. The CNT/PDMS CCF exhibited excellent compression performance and stable electrical response signals. The CCF-based piezoresistive sensor can effectively detect compression strain down to 0.1% and shows excellent and stable response behavior under compression strain up to 90%. In addition, the CCF demonstrates excellent fast response and recovery times (54 ms and 65 ms), as well as durability and stability (2000 cycles). The CCF-based piezoresistive sensors can be applied to monitor human movement and weak physiological signals. The artificial electronic skin integrated with CCF can be applied to human-computer intelligent interaction. In addition, The CCF also can be involved in roughness recognition, optical and thermal sensing, indicating its great potential application in environmental monitoring.

Declaration of Competing Interest

The authors declare that they have no known competing financial interests or personal relationships that could have appeared to influence the work reported in this paper.

Data availability

Data will be made available on request.

Appendix A. Supporting information

Supplementary data associated with this article can be found in the online version at [doi:10.1016/j.sna.2023.114408](https://doi.org/10.1016/j.sna.2023.114408).

References

- [1] X. Bai, Y. Du, C. Gai, Y. Guo, Y. Liu, Y. Huang, H. Xu, D. Wu, J. Sun, Secondary embossing method for the encapsulation of high-sensitive flexible piezoresistive sensors, *Sens. Actuators A Phys.* 335 (2022) 113356, <https://doi.org/10.1016/j.sna.2021.113356>.
- [2] G. Gilanizadehdizaj, K.C. Aw, J. Stringer, D. Bhattacharyya, Facile fabrication of flexible piezo-resistive pressure sensor array using reduced graphene oxide foam and silicone elastomer, *Sens. Actuators A Phys.* 340 (2022) 113549, <https://doi.org/10.1016/j.sna.2022.113549>.
- [3] M.A.U. Khalid, S.H. Chang, Flexible strain sensors for wearable applications fabricated using novel functional nanocomposites: A review, *Compos. Struct.* 284 (2022), 115214, <https://doi.org/10.1016/j.comstruct.2022.115214>.
- [4] X. Wang, J. Yu, Y. Cui, W. Li, Research progress of flexible wearable pressure sensors, *Sens. Actuator A Phys.* 330 (2021), 112838, <https://doi.org/10.1016/j.sna.2021.112838>.
- [5] F. Yuan, Y. Xia, Q. Lu, Q. Xu, Y. Shu, X. Hu, Recent advances in inorganic functional nanomaterials based flexible electrochemical sensors, *Talanta* 244 (2022), 123419, <https://doi.org/10.1016/j.talanta.2022.123419>.
- [6] K. Singh, S. Sharma, M. Gupta, C.C. Tripathi, Fabrication of serpentine and I structured graphene-CNT based highly sensitive and flexible strain sensors, *Microelectron. Eng.* 250 (2021), 111631, <https://doi.org/10.1016/j.mee.2021.111631>.
- [7] H. Xue, J. Hu, A liquid power-ultrasound based green fabrication process for flexible strain sensors at room temperature and normal pressure, *Sens. Actuator A Phys.* 329 (2021), 112822, <https://doi.org/10.1016/j.sna.2021.112822>.
- [8] Y. Ren, L. Qing, L. Li, Hasichaolu, H. Zheng, K. Ou, Facile synthesis of highly conductive polymer fiber for application in flexible fringing field capacitive sensor, *Sens. Actuators A Phys.* 342 (2022), 113616, <https://doi.org/10.1016/j.sna.2022.113616>.
- [9] Y. Wang, Z. Chen, D. Mei, L. Zhu, S. Wang, X. Fu, Highly sensitive and flexible tactile sensor with truncated pyramid-shaped porous graphene/silicone rubber composites for human motion detection, *Compos. Sci. Technol.* 217 (2022), 109078, <https://doi.org/10.1016/j.compscitech.2021.109078>.
- [10] Y. Jung, K.K. Jung, D.H. Kim, D.H. Kwak, S. Ahn, J.S. Han, J.S. Ko, Flexible and highly sensitive three-axis pressure sensors based on carbon nanotube/polydimethylsiloxane composite pyramid arrays, *Sens. Actuators A Phys.* 331 (2021), 113034, <https://doi.org/10.1016/j.sna.2021.113034>.
- [11] S. Nuthalapati, V. Shirhatti, V. Kedambaimoole, V. Pandi N, H. Takao, M.M. Nayak, K. Rajanna, Highly sensitive flexible strain and temperature sensors using solution processed graphene palladium nanocomposite, *Sens. Actuator A Phys.* 334 (2022), 113314, <https://doi.org/10.1016/j.sna.2021.113314>.
- [12] J. Zhu, X. Xue, J. Li, J. Wang, H. Wang, Y. Xing, P. Zhu, Flexible pressure sensor with a wide pressure measurement range and an agile response based on multiscale carbon fibers/carbon nanotubes composite, *Microelectron. Eng.* 257 (2022), 111750, <https://doi.org/10.1016/j.mee.2022.111750>.
- [13] F. Wang, Y. Tan, H. Peng, F. Meng, X. Yao, Investigations on the preparation and properties of high-sensitive BaTiO₃/MwCNTs/PDMS flexible capacitive pressure sensor, *Mater. Lett.* 303 (2021), 130512, <https://doi.org/10.1016/j.matlet.2021.130512>.
- [14] X. Zhou, Z. Gong, J. Fan, Y. Chen, Self-healable, recyclable, mechanically tough transparent polydimethylsiloxane elastomers based on dynamic microphase separation for flexible sensor, *Polymer* 237 (2021), 124357, <https://doi.org/10.1016/j.polymer.2021.124357>.
- [15] B. Li, W. Liang, L. Zhang, F. Ren, F. Xuan, TPU/CNTs flexible strain sensor with auxetic structure via a novel hybrid manufacturing process of fused deposition modeling 3D printing and ultrasonic cavitation-enabled treatment, *Sens. Actuators A Phys.* 340 (2022), 113526, <https://doi.org/10.1016/j.sna.2022.113526>.
- [16] R. Li, Q. Zhou, Y. Bi, S. Cao, X. Xia, A. Yang, S. Li, X. Xiao, Research progress of flexible capacitive pressure sensor for sensitivity enhancement approaches, *Sens. Actuators A Phys.* 321 (2021), 112425, <https://doi.org/10.1016/j.sna.2020.112425>.
- [17] C.R. Yang, L.J. Wang, S.F. Tseng, Arrayed porous polydimethylsiloxane/barium titanate microstructures for high-sensitivity flexible capacitive pressure sensors, *Ceram. Int.* 48 (2022) 13144–13153, <https://doi.org/10.1016/j.ceramint.2022.01.191>.
- [18] B. Xu, F. Ye, R. Chen, X. Luo, G. Chang, R. Li, A wide sensing range and high sensitivity flexible strain sensor based on carbon nanotubes and MXene, *Ceram. Int.* 48 (2022) 10220–10226, <https://doi.org/10.1016/j.ceramint.2021.12.235>.
- [19] W. Li, X. Jin, X. Han, Y. Li, W. Wang, T. Lin, Z. Zhu, Synergy of porous structure and microstructure in piezoresistive material for high-performance and flexible pressure sensors, *ACS Appl. Mater. Interfaces* 13 (2021) 19211–19220, <https://doi.org/10.1021/acsmami.0c22938>.
- [20] R. Li, Q. Zhou, Y. Bi, S. Cao, X. Xia, A. Yang, S. Li, X. Xiao, Research progress of flexible capacitive pressure sensor for sensitivity enhancement approaches, *Sens. Actuators A Phys.* 321 (2021), 112425, <https://doi.org/10.1016/j.sna.2020.112425>.
- [21] J. Hwang, Y. Kim, H. Yang, J. Oh, Fabrication of hierarchically porous structured PDMS composites and their application as a flexible capacitive pressure sensor, *Compos. B. Eng.* 211 (2021), 108607, <https://doi.org/10.1016/j.compositesb.2021.108607>.
- [22] T. Mulembo, G. Nagai, H. Tamagawa, T. Nitta, M. Sasaki, Conductive and flexible multi-walled carbon nanotube/polydimethylsiloxane composites made with naphthalene/toluene mixture, *J. Appl. Polym. Sci.* 136 (2019) 48167, <https://doi.org/10.1002/app.48167>.
- [23] Z. Sang, K. Ke, Ica Manas-Zloczower, Design strategy for porous composites aimed at pressure sensor application, *Small* 15 (2019) 1903487, <https://doi.org/10.1002/smll.201903487>.
- [24] Y. Wan, N. Qin, Y. Wang, Q. Zhao, Q. Wang, P. Yuan, Q. Wen, H. Wei, X. Zhang, N. Ma, Sugar-templated conductive polyurethane-polyppyrrole sponges for wide-range force sensing, *Chem. Eng. J.* 383 (2020), 123103, <https://doi.org/10.1016/j.cej.2019.123103>.
- [25] X. Tang, C. Wu, L. Gan, T. Zhang, T. Zhou, J. Huang, H. Wang, C. Xie, D. Zeng, Multilevel microstructured flexible pressure sensors with ultrahigh sensitivity and

- ultrawide pressure range for versatile electronic skins, *Small* 15 (2019) 1804559, <https://doi.org/10.1002/smll.201804559>.
- [26] Y. He, M. Zhou, M. Mahmoud, X. Lu, G. He, L. Zhang, M. Huang, A. Elnaggar, Q. Lei, H. Liu, C. Liu, I. Azab, Multifunctional wearable strain/pressure sensor based on conductive carbon nanotubes/silk nonwoven fabric with high durability and low detection limit, *Adv. Compos. Hybrid. Mater* 5 (2022) 1939–1950, <https://doi.org/10.1007/s42114-022-00525-z>.
- [27] L. Ma, X. Lei, S. Li, S. Guo, J. Yuan, X. Li, G.J. Cheng, F. Liu, A 3D flexible piezoresistive sensor based on surface-filled graphene nanosheets conductive layer, *Sens. Actuators A Phys.* 332 (2021), 113144, <https://doi.org/10.1016/j.sna.2021.113144>.
- [28] H. Liu, M. Dong, W. Huang, J. Gao, K. Dai, J. Guo, G. Zheng, C. Liu, C. Shen, Z. Guo, Lightweight conductive graphene/thermoplastic polyurethane foams with ultrahigh compressibility for piezoresistive sensing, *J. Mater. Chem. C* 5 (2017) 73–83, <https://doi.org/10.1039/c6tc03713e>.
- [29] D. Fu, R. Wang, Y. Wang, Q. Sun, C. Cheng, X. Guo, R. Yang, An easily processable silver nanowires-dual-cellulose conductive paper for versatile flexible pressure sensors, *Carbohydr. Polym.* 283 (2022), 119135, <https://doi.org/10.1016/j.carbpol.2022.119135>.
- [30] X. Cui, J. Chen, W. Wu, Y. Liu, H. Li, Z. Xu, Y. Zhu, Flexible and breathable all-nanofiber iontronic pressure sensors with ultraviolet shielding and antibacterial performances for wearable electronics, *Nano Energy* 95 (2022), 107022, <https://doi.org/10.1016/j.nanoen.2022.107022>.
- [31] Z. Zhang, L. Wang, K. Guo, L. Guan, X. Wang, Z. Wu, Durable and highly sensitive flexible sensors for wearable electronic devices with PDMS-MXene/TPU composite films, *Ceram. Int.* 48 (2022) 4977–4985, <https://doi.org/10.1016/j.ceramint.2021.11.035>.
- [32] X. Lei, L. Ma, Y. Li, Y. Cheng, G.J. Cheng, F. Liu, Highly sensitive and wide-range flexible pressure sensor based on carbon nanotubes-coated polydimethylsiloxane foam, *Mater. Lett.* 308 (2022), 131151, <https://doi.org/10.1016/j.matlet.2021.131151>.
- [33] Y. He, D. Wu, M. Zhou, Y. Zheng, T. Wang, C. Lu, L. Zhang, H. Liu, C. Liu, Wearable strain sensors based on a porous polydimethylsiloxane hybrid with carbon nanotubes and graphene, *ACS Appl. Mater. Interfaces* 13 (2021) 15572–15583, <https://doi.org/10.1021/acsami.0c22823>.
- [34] B. Arman Kuzubasoglu, S.Kursun Bahadir, Flexible temperature sensors: A review, *Sens. Actuators A Phys.* 315 (2020), 112282, <https://doi.org/10.1016/j.sna.2020.112282>.
- [35] Q. Zhang, L. Shen, P. Liu, P. Xia, J. Li, H. Feng, C. Liu, K. Xing, A. Song, M. Li, X. Yang, Y. Huang, Highly sensitive resistance-type flexible pressure sensor for cuffless blood-pressure monitoring by using neural network techniques, *Compos. B. Eng.* 226 (2021), 109365, <https://doi.org/10.1016/j.compositesb.2021.109365>.
- [36] L. Wang, T. Xu, X. Zhang, Multifunctional conductive hydrogel-based flexible wearable sensors, *TrAC Trends Anal. Chem.* 134 (2021), 116130, <https://doi.org/10.1016/j.trac.2020.116130>.
- [37] R. Qin, X. Li, M. Hu, G. Shan, R. Seeram, M. Yin, Preparation of high-performance MXene/PVA-based flexible pressure sensors with adjustable sensitivity and sensing range, *Sens. Actuators A Phys.* 338 (2022), 113458, <https://doi.org/10.1016/j.sna.2022.113458>.
- [38] S. Peng, Q. Guo, N. Thirunavukkarasu, Y. Zheng, Z. Wang, L. Zheng, L. Wu, Z. Weng, Tailoring of photocurable ionogel toward high resilience and low hysteresis 3D printed versatile porous flexible sensor, *Chem. Eng. J.* 439 (2022), 135593, <https://doi.org/10.1016/j.cej.2022.135593>.
- [39] Y. He, Q. Chen, H. Liu, L. Zhang, D. Wu, C. Lu, W. OuYang, D. Jiang, M. Wu, J. Zhang, Y. Li, J. Fan, C. Liu, Z. Guo, Friction and wear of MoO₃/graphene oxide modified glass fiber reinforced epoxy nanocomposites, *Mater. Eng.* 304 (2019) 1970018, <https://doi.org/10.1002/mame.201970018>.
- [40] G. Yang, X. Tang, G. Zhao, Y. Li, C. Ma, X. Zhuang, J. Yan, Highly sensitive, direction-aware, and transparent strain sensor based on oriented electrospun nanofibers for wearable electronic applications, *Chem. Eng. J.* 435 (2022), 135004, <https://doi.org/10.1016/j.cej.2022.135004>.
- [41] V. Sankar, K. Balasubramaniam, R. Sundara, Insights into the effect of polymer functionalization of multivalued carbon nanotubes in the design of flexible strain sensor, *Sens. Actuator A Phys.* 322 (2021), 112605, <https://doi.org/10.1016/j.sna.2021.112605>.
- [42] P. Song, G. Wang, Y. Zhang, Preparation and performance of graphene/carbon black silicone rubber composites used for highly sensitive and flexible strain sensors, *Sens. Actuators A Phys.* 323 (2021), 112659, <https://doi.org/10.1016/j.sna.2021.112659>.
- [43] N. Athti, W. Sriputkhai, P. Pattamang, O. Thongsook, R. Meananeatrat, P. Saengdee, A. Srihapat, J. Supadech, T. Janseng, A. Maneesong, N. Kongto, A. Rodchanarowan, N. Klunngien, W. Jeamsaksiri, Superhydrophobic and superoleophobic properties enhancement on PDMS micro-structure using simple flame treatment method, *Microelectron. Eng.* 230 (2020), 111362, <https://doi.org/10.1016/j.mee.2020.111362>.
- [44] S. Nuthalapati, V. Shirhatti, V. Kedambamoole, V. Pandi N, H. Takao, M.M. Nayak, K. Rajanna, Highly sensitive flexible strain and temperature sensors using solution processed graphene palladium nanocomposite, *Sens. Actuators A Phys.* 334 (2022), 113314, <https://doi.org/10.1016/j.sna.2021.113314>.
- [45] Y. Lin, Q. Yin, L. Ding, G. Yuan, H. Jia, J. Wang, Ultra-sensitive flexible strain sensors based on hybrid conductive networks for monitoring human activities, *Sens. Actuators A Phys.* 342 (2022), 113627, <https://doi.org/10.1016/j.sna.2022.113627>.
- [46] Y. He, Q. Chen, D. Wu, M. Zhou, T. Wang, C. Lu, L. Zhang, H. Liu, C. Liu, Effect of multiscale reinforcement by fiber surface treatment with polyvinyl alcohol/graphene oxide/oxidized carbon nanotubes on the mechanical properties of reinforced hybrid fiber composites, *Compos. Sci. Technol.* 204 (2021), 108634, <https://doi.org/10.1016/j.compscitech.2020.108634>.
- [47] S. Kim, B. Yoo, M. Miller, D. Bowen, D.J. Pines, K.M. Daniels, EGaIn-Silicone-based highly stretchable and flexible strain sensor for real-time two joint robotic motion monitoring, *Sens. Actuators A Phys.* 342 (2022), 113659, <https://doi.org/10.1016/j.sna.2022.113659>.
- [48] Y. Yin, Y. Wang, H. Li, J. Xu, C. Zhang, X. Li, J. Cao, H. Feng, G. Zhu, A flexible dual parameter sensor with hierarchical porous structure for fully decoupled pressure–temperature sensing, *Chem. Eng. J.* 430 (2022), 133158, <https://doi.org/10.1016/j.cej.2021.133158>.
- [49] C. Ryu, S. Hajra, M. Sahu, S.I. Jung, I.R. Jang, H.J. Kim, PVDF-bismuth titanate based self-powered flexible tactile sensor for biomechanical applications, *Mater. Lett.* 309 (2022), 131308, <https://doi.org/10.1016/j.matlet.2021.131308>.
- [50] N. Jiang, X. Chang, D. Hu, L. Chen, Y. Wang, J. Chen, Y. Zhu, Flexible, transparent, and antibacterial ionogels toward highly sensitive strain and temperature sensors, *Chem. Eng. J.* 424 (2021), 130418, <https://doi.org/10.1016/j.cej.2021.130418>.
- [51] J. Tie, Z. Mao, L. Zhang, Y. Zhong, X. Sui, H. Xu, Conductive ionogel with underwater adhesion and stability as multimodal sensor for contactless signal propagation and wearable devices, *Compos. B. Eng.* 232 (2022), 109612, <https://doi.org/10.1016/j.compositesb.2022.109612>.
- [52] X. Guo, L. Ma, W. Wu, S. Li, X. Lei, X. Wu, X. Yu, F. Liu, Ultra-sensitive flexible piezoresistive pressure sensor prepared by laser-assisted copper template for health monitoring, *Sens. Actuators A Phys.* 334 (2022), 113325, <https://doi.org/10.1016/j.sna.2021.113325>.
- [53] R. Mao, W. Yao, A. Qadir, W. Chen, W. Gao, Y. Xu, H. Hu, 3-D graphene aerogel sphere-based flexible sensors for healthcare applications, *Sens. Actuators A Phys.* 312 (2020), 112144, <https://doi.org/10.1016/j.sna.2020.112144>.
- [54] Y. Yang, W. Zhou, X. Chen, J. Ye, H. Wu, A flexible touching sensor with the variation of electrical impedance distribution, *Measurement* 183 (2021), 109778, <https://doi.org/10.1016/j.measurement.2021.109778>.
- [55] Z. Wang, Z. Yao, C. Li, J. Lv, H. Fu, Z.P. Mourelatos, A new fluctuation assessment method for the step response signals of pressure sensors, *Mech. Syst. Signal Pract.* 118 (2019) 1–12, <https://doi.org/10.1016/j.ymssp.2018.08.035>.
- [56] Q. Zou, Z. Lei, T. Xue, S. Li, Z. Ma, Q. Su, Highly sensitive flexible pressure sensor based on ionic dielectric layer with hierarchical ridge microstructure, *Sens. Actuators A Phys.* 313 (2020), 112218, <https://doi.org/10.1016/j.sna.2020.112218>.
- [57] N. Wang, H. Sun, X. Yang, W. Lin, W. He, H. Liu, G. Bhat, B. Yu, Flexible temperature sensor based on RGO/CNTs@PBT melting blown nonwoven fabric, *Sens. Actuators A Phys.* 339 (2022), 113519, <https://doi.org/10.1016/j.sna.2022.113519>.
- [58] J. Luo, L. Zhang, T. Wu, H. Song, C. Tang, Flexible piezoelectric pressure sensor with high sensitivity for electronic skin using near-field electrohydrodynamic direct-writing method, *Extrem. Mech. Lett.* 48 (2021), 101279, <https://doi.org/10.1016/j.eml.2021.101279>.
- [59] R. Chen, T. Luo, D. Geng, Z. Shen, W. Zhou, Facile fabrication of a fast-response flexible temperature sensor via laser reduced graphene oxide for contactless human-machine interface, *Carbon* 187 (2022) 35–46, <https://doi.org/10.1016/j.carbon.2021.10.064>.
- [60] G. Zhu, F. Wang, L. Chen, C. Wang, Y. Xu, J. Chen, X. Chang, Y. Zhu, Highly flexible TPU/SWCNTs composite-based temperature sensors with linear negative temperature coefficient effect and photo-thermal effect, *Compos. Sci. Technol.* 217 (2022), 109133, <https://doi.org/10.1016/j.compscitech.2021.109133>.
- [61] H. Zhou, Z. Jin, Y. Gao, P. Wu, J. Lai, S. Li, X. Jin, H. Liu, W. Chen, Y. Wu, A. Ma, Thermoresponsive, magnetic, adhesive and conductive nanocomposite hydrogels for wireless and non-contact flexible sensors, *Colloid Surf. A* 636 (2022), 128113, <https://doi.org/10.1016/j.colsurfa.2021.128113>.
- [62] X. Cui, J. Chen, Y. Zhu, W. Jiang, Lightweight and conductive carbon black/chlorinated poly(propylene carbonate) foams with a remarkable negative temperature coefficient effect of resistance for temperature sensor applications, *J. Mater. Chem. C* 6 (2018) 9354–9362, <https://doi.org/10.1039/C8TC02123F>.



Yuxin He is an Associate Professor of Materials Science and Engineering, Henan University of Science and Technology. He obtained his Ph.D. degree from Shaanxi University of Science and Technology (2009), and worked as a post-doctoral at Key Laboratory of Materials Processing and Mold (Zhengzhou University). His current research interest focuses on the multifunctional polymer-based nanocomposites and fiber reinforced polymer-based composites.